Lian, Junhe; Koch, Marco; Li, Wei; Wierzbicki, Tomasz; Zhu, Juner

Mechanical Deformation of Lithium-Ion Pouch Cells under in-plane Loads-Part II

Published in:
Journal of the Electrochemical Society

DOI:
10.1149/1945-7111/ab9eee

Published: 07/01/2020

Document Version
Publisher's PDF, also known as Version of record

OPEN ACCESS

Mechanical Deformation of Lithium-Ion Pouch Cells under in-plane Loads—Part II: Computational Modeling

Journal of The Electrochemical Society, 2020 **167** 090556

Mechanical Deformation of Lithium-Ion Pouch Cells under in-plane Loads—Part II: Computational Modeling

Junhe Lian,[1,2,z] Marco Koch,[2,3] Wei Li,[2] Tomasz Wierzbicki,[2] and Juner Zhu[2,z]

[1]*Advanced Manufacturing and Materials, Department of Mechanical Engineering, Aalto University, 02150 Espoo, Finland*
[2]*Impact and Crashworthiness Lab, Department of Mechanical Engineering, Massachusetts Institute of Technology, Cambridge, Massachusetts 02139-4307, United States of America*
[3]*Production Engineering of E-Mobility Components, RWTH Aachen University, 52056 Aachen, Germany*

Based on the experimental observation, pouch cells can withstand severe deformation during fully confined in-plane compression with flat punches without any risks of a short circuit. During the deformation, the structuralbehavior is characterized by regular kinks, buckles, and shear bands. This study aims to provide a modeling approach for the in-plane compression on lithium-ion pouch batteries in a fully confined case with a flat punch. To capture the right mechanism of buckling while maintaining a satisfactory computational efficiency, two approaches are proposed: a homogenized model with imperfections and an enhanced homogenized model with equivalent layers of metal foils. The first approach introduces periodic geometrical imperfections with a wavelength as observed in the experiments. The second one creates a model in between the homogenized model and detailed model with equivalent properties of coating materials and metal foils. It is concluded that the introduction of imperfections could not correctly capture the folding mechanism, while with the latter hybrid approach, it is possible to capture the right progressive folding pattern of the battery cells during the in-plane compression test. Different potential approaches of the simulation model are investigated for obtaining a better agreement of the prediction and the measured experimental load-displacement response.
 [DOI: 10.1149/1945-7111/ab9eee]

Manuscript submitted March 23, 2020; revised manuscript received June 11, 2020. Published June 30, 2020. *This paper is part of the JES Focus Issue on Battery Safety, Reliability and Mitigation.*

The increasing need for mobility is in direct conflict with the global challenges of finite fossil fuels and the advancing climate change. Therefore, battery electric vehicles (EV) have been pursued by many countries worldwide due to its advantages in reducing the dependency on oil as well as in its clean emission to the environment if batteries are charged with electricity from renewable sources. Increasing the energy density of lithium-ion batteries is essential for increasing the range and thus sustainably establishing the electromobility. There are three established form factors of cells on the market: pouch, cylindrical, and prismatic. The pouch cell is perhaps the most promising in terms of increasing the energy density because of its compact design. However, with respect to the safety of electric vehicles, the low mechanical resistance and a possible expansion due to aging caused by gas development are its disadvantages. They get even more significant considering the fact that the battery packs may undergo large plastic deformation during EV crash accidents.[1]

To guarantee the mechanical safety of the battery cells, especially in various accidents for electric vehicles, different types of mechanical abuse tests have been designed and conducted. Most of these tests cause out-of-plane deformation of the pouch cells, such as the hemispherical and cylindrical indentation tests, uniaxial unconstrained and partially/fully confined compression tests, and three-point bending tests.[2–9] One of the probably most known tests is the nail penetration test. In order to make it comparable, many parameters are fixed during the test. The nail must consist of steel, have a diameter of 3 mm, and be orientated perpendicular to cell electrodes. The penetration itself should go through the cell and with a minimum speed of 8 cm/second. This type of mechanical loads can cause one of the most critical accident scenarios and has, therefore, been widely used as a standard test for the study of thermal runaway.[10]

Extensive out-of-plane tests and simulations have been performed, but significantly fewer in-plane tests have been conducted. Especially few tests were conducted on real commercial batteries with applications in the automotive industry. Up to now, among the vast mechanical abuse tests performed in the literature, only less than ten studies focusing on the in-plane compression[8,11–18] but with small pouch cells were performed. However, pouch cells are oftentimes forced to be compressed in the in-plane direction in various crash tests, as in most cases they are stacked parallel in modules and placed vertically to the ground. Therefore, the in-depth understanding of automotive and cell manufacturers regarding the mechanical deformation of lithium-ion pouch cells during in-plane compression is focused in this study.

The motivation behind testing the mechanical property of the batteries is on one hand to understand the mechanical behavior and how it leads to a battery failure and on the other hand to create and validate computational battery models. The pouch battery cells consist of a complex assembly of alternating active material coated current collectors and separator layers as well as the cell enclosure (pouch). With the development of experimental data of all the components of a lithium-ion battery and their interaction with one another, it is possible to develop a very detailed finite element model with all properties. There have already been developed detailed models for various battery cells.[11,19–21] These models are especially helpful when investigating the deformation behavior of the cell structure as well as how and where short circuits happen.[22] However, this method requires a significant amount of computational resources, as the detailed models of an EV battery cell could have millions of elements with a proper resolution of the layers and deformation. This is a challenge of such models to be applied to large pouch cells for both out-of-plane and in-plane deformation.

To compensate for the high computational effort of the detailed model, representative volume element (RVE) models are developed for measurements of an entire cell that can be represented by a small repeatable unit.[23] It has been proven to be a very efficient method in the metal forming society to link the microstructure with various mechanical properties, such as stresses,[24,25] plastic anisotropy,[26,27] and damage behavior.[28–30] Sahraei et al.,[31] Lai et al.,[15] and Zhang et al.[32] used the same fundamental structure, one RVE consisting out of one copper and aluminum foil with an active material coating on both sides and a separator in between and at the bottom. With these models, the deformation mechanism of the cell can be investigated as there are much fewer elements in an RVE model than in a detailed model and therefore the computational effort is much smaller. However, due to the periodic boundary conditions and small strain gradients, the use of such models is also limited. If cylindrical punch

[z]E-mail: junhe.lian@aalto.fi; zhujuner@mit.edu

tests or three-point-bending tests are performed, the stress field within the battery is inhomogeneous in different axes, which makes it very difficult to get a good definition of the boundary conditions of the RVE. When the boundary conditions are not defined properly, there is a risk that the RVE shows a size effect on its mechanical behavior, which has been studied by changing the ratio of compression and tension in two directions by Sahraei et al.[31] Furthermore, the stress–strain curve can be obtained from the RVE model.[15] To get better results the model should be calibrated separately either for tension or for compression.[32] As for the detailed model factors like contact pressure, adhesion and friction still need to be investigated properly.

On the contrary, homogenized models treat the entire battery cell as a continuum medium and constitutive equations are developed to represent the deformation behavior of the cells. Due to this simplification, it is among all computational modeling strategies the most efficient one and has been also applied to many mechanical abuse tests. Two typical homogenized models are the crushable foam model in LS-DYNA,[7,9] and the Deshpande–Fleck model in Abaqus.[1,33] Such models can predict the global force–displacement response of various cells with good accuracy. To also enable its prediction on the failure of battery cells, Sahraei et al.[6] proposed the criterion based on the critical value of the maximum principal strain. In a more recent study, Lian et al.[34] compared seven different failure criteria for the rod indentation tests by evaluating the force–-displacement responses as well as the failure patterns. It is concluded that two mixed stress–strain based criteria, the Cockcroft–Latham and Johnson–Cook, both performed the best.

The purpose of our present study is to fill the above gaps by diving deeply into the in-plane deformation of a large-format pouch battery cell. In this investigation, both experimental tests and numerical simulations will be reported in two publications. Part I[35] describes the details of the experimental investigations, which will be further used by the present Part II for developing a numerical model for characterization. There is sufficient experimental evidence, described in the experimental part[35] that buckling is a dominant deformation mode in pouch cells subjected to in-plane compression. It is a characteristic deformation pattern of slender structures. Pouch, and even more prismatic cells are not slender. So, where is buckling coming from, and what is the mechanics of the deformation process?

The detailed mechanical model developed by the present investigating team[19] provides the correct physical answer in terms of the observed deformation pattern. All major components of the jelly roll are extremely slender. They are allowed to slide with respect to each other and delaminate in tension. The compressible coating acts as a crushable foundation. So the system behaves as a plate or beam on a foundation and develops local buckling, according to classical structural mechanics. The buckling process is controlled by structural imperfections.

However, as described before, the detailed finite element (FE) model of cells is prohibitively expensive to run in the industrial environment. The challenge is how to include the right physics of the problem in a homogenized model, which has become the industry standard for battery simulations. Two approaches are proposed here. In the first approach, the homogenized model will be used. However, it is obvious that the homogenized model could experience difficulty to render these folds correctly. Therefore, the regular FE mesh in the homogenized model is distorted by structural imperfections.[36] In the present paper, periodic geometrical imperfections are introduced with a wavelength comparable to the cell thickness. The size of the imperfection is considered as a parameter in the sensitivity study. The second one is a hybrid model where a few slender members are inserted into the homogenized model. Each insert represents several aluminum and copper foils lumped together. These members buckle as plates on foundations, initiating the buckling and folding process of the entire cell. Such a model could, on the one hand, capture the deformation physics during the tests and on the other hand, preserve computational efficiency. Both approaches are described in the subsequent sections of the paper.

Numerical Modeling

Overall methodology.—In the present numerical work, only the fully confined in-plane compression tests are focused on. As shown in the Part I study,[35] the tests show a clear progressive folding

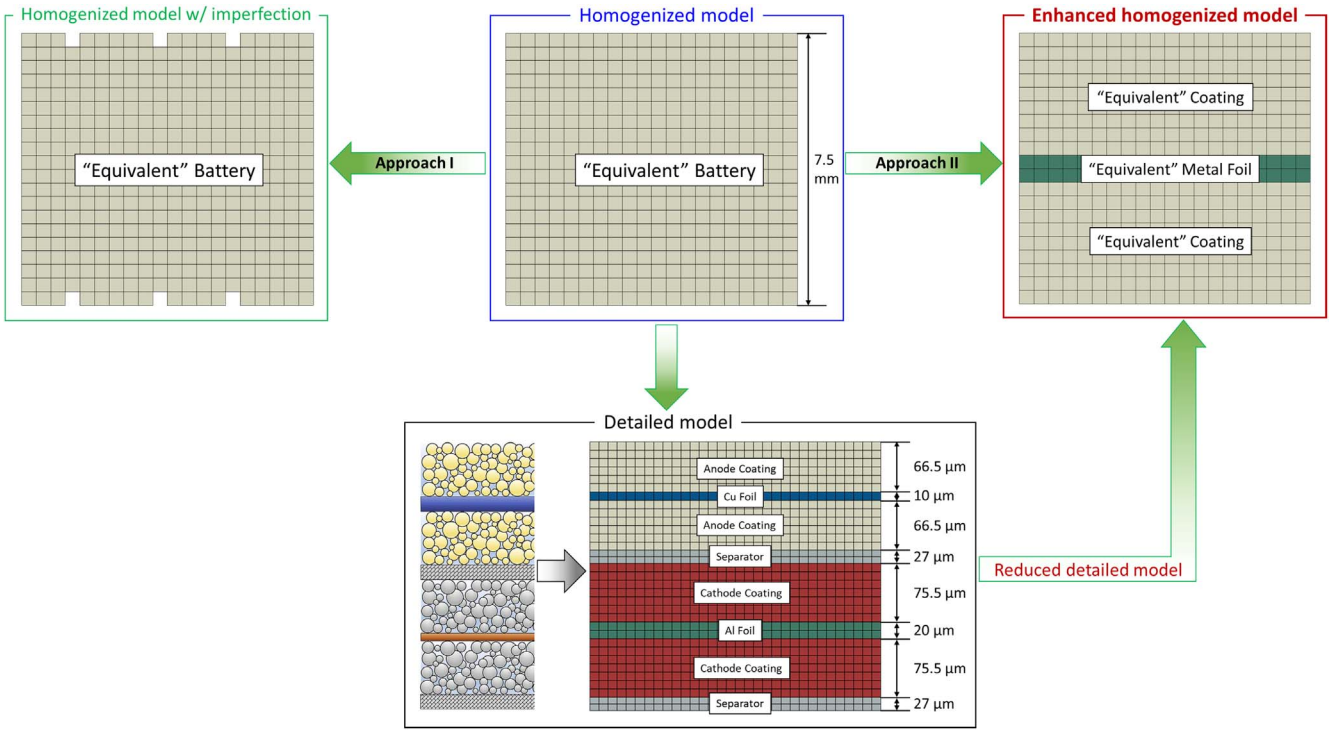

Figure 1. The concept of the two approaches in the present study to trigger buckling during the in-plane compression test simulation, Approach I: homogenized model with imperfections and Approach II: "enhanced homogenized model."

pattern during deformation. This feature affects also significantly the force–displacement response of the batteries. In the sense of numerical simulations, the test is a proper candidate to validate the plastic model and to examine the anisotropic deformation behavior of the batteries. However, the folding behavior and its influence on the force challenge the use of a homogenized model, as material inhomogeneity is a necessity to capture the right number of the folds, accordingly the right level of force–displacement responses. Therefore, in addition to the completely homogenized model, in this study, two approaches are implemented as shown in Fig. 1. The first approach will introduce periodic geometrical imperfections into the homogenized model with the wavelength equal to the experimentally measured values. The size of imperfections will be subjected to a sensitivity study.

In the second approach, different layers of metal foils are also added to trigger the progressive folding during deformation. Ideally, a detailed model with the exact number of coating materials and Al and Cu foils as well as separators would provide the most physical solution. However, it would require a significant amount of computational effort due to the very thin layers of different materials, only about 10 microns for the copper foil, resulting in about 15 million elements in even 2D conditions, which would beyond the calculation capability for modern computer workstations. Therefore, in this study, the concept of a "**reduced detailed model**" or "**enhanced homogenized model**" is introduced to on the one hand provide the necessary and the right number of folds during deformation and on the other hand reduce the computational effort essentially. This concept is shown in Fig. 1. For the implementation of the concept, the following assumptions are made:

(i) The five repeating materials of the batteries in a detailed model (coating materials in cathode and anode, Al foil, Cu foil, and separator) are simplified into "equivalent" coating material and "equivalent" metal foil;
(ii) The deformation of the "equivalent" coating material follows the Deshpande–Fleck foam model, while the "equivalent" metal foil follows the J2 Mises plasticity model;
(iii) The volume fraction of the "equivalent" metal foil is calculated as the sum of the fraction of Al and Cu foils and this fraction is kept constant, while the number of the "equivalent" metal foils is varied;
(iv) The "equivalent" metal foil is always placed at the center of the battery and spread towards the surfaces;
(v) The hardening curve of the "equivalent" metal foil is the equivalent one of the Al and Cu foils weighted by their relative volume ratio (detailed calibration is given in the next section);
(vi) The hardening behavior of the "equivalent" coating material is optimized with the obtained "equivalent" metal foil properties and the overall deformation behavior of the battery under the out-of-plane indentation test by a flat punch. The details are provided in the next section.

With these assumptions, the models and their relevant material properties can be obtained, which will be shown in the following sections. In addition to the number of foils, another influencing parameter is the contact between the metal foils and coating materials. In the current study, contact is applied between the metal and coating materials but without any friction.

Model setup.—The battery to be simulated is the 26.3 Ah large-format pouch cell with $LiMn_2O_4$(LMO)/$LiNi_1/3Co_1/3Mn_1/3O_2$(NCM111)-graphite chemistry and carbonate-based liquid electrolyte by LG Chem. The dimension of the cell is 195 mm × 150 mm × 7.5 mm and we focus only on the fully-confined in-plane compression tests as reported in detail in Part I paper for the experimental results. The finite element model of the in-plane compression test is set up in Abaqus/Explicit. The overview of the model is shown in Fig. 2. A 3D model is constructed with one symmetry along the longitudinal direction of the battery. The two side cover steel plates are modeled as rigid bodies without any possible degree of freedom for translating or rotating. The flat punch and the testing ground are also modeled as rigid bodies. The testing ground is fixed in all degrees of freedom, while the flat punch is also fixed in the same way except a horizontal movement (vertical direction in test) to mimic the experiments. The battery cell is placed in the center between the two side plates with an overall gap of 1.6 mm, 0.8 mm for each side. For the homogenized model, the battery is in contact with all the four rigid bodies during the test and frictionless condition is assumed. For the enhanced homogenized model, except for the contact to the rigid bodies, the layers also have contacts and relative moves. The same frictionless contact is assumed between the layers. The model is set up in a quasi-static condition to be compared with the experimental loading. Time scaling is used to speed up the simulation but very minimal kinetic energy is introduced compared to the internal energy and no mass-scaling is used in the model.

For the two modeling approaches introduced above, the zoom-in view of the FE models is shown in Figs. 3 and 4. For both cases, 3D continuum brick elements with reduced integration points (C3D8R) from Abaqus/Explicit are used. In the homogenized model with imperfections, 11 pairs of periodic geometrical imperfections are implemented, the same as the experimental observation. Two sizes of the imperfections are considered, "small" with a size of 0.5 mm × 0.25 mm and "large" with a size of 0.5 mm × 0.5 mm.

For the enhanced homogenized model, five cases with different numbers of the metal foils are detailed. According to the dimension of the different components in the pouch cell described in Part I paper and illustrated in Fig. 1, the volume fraction of the "equivalent" metal foils is 8.15%. This fraction is kept always constant while the layers are varied for 1, 3, 5, 7, and 15. It is noted that layer number 15 is introduced to validate the convergence of the force–displacement response and the folding response of the in-plane compression. Accordingly, the thickness of each layer is decreased. As one of the assumptions, the first layer of the metal foil is always placed at the center of the battery and they are spread toward the surface. Therefore, the surface layers of the battery are always the "equivalent" coating materials. The repeating unit of the cell is a sandwich structure with two layers of coating materials and one layer of metal foil in the middle. Accordingly, when two repeating units are in contact, there is also contact between the two adjacent coating materials. The same frictionless condition is applied here as well. A coarse mesh is applied with the edge element size of 0.5 mm.

Constitutive Models

Deshpande–Fleck foam model.—The Deshpande–Fleck model[37] is employed for the description of the homogenized deformation behavior of the equivalent coating materials of batteries. As fracture was not found in the experiments, the failure criterion described in the previous study[34] was not included here. The fundamental equations of the model are briefly described below. For a more detailed description of the model and its extension to failure prediction, the readers are referred to the previous study from the group.[34]

The Deshpande–Fleck yield function is expressed as:

$$\Phi = \sqrt{q^2 + \alpha^2\left[p - \frac{p_c - p_t}{2}\right]^2} - \alpha\frac{p_c + p_t}{2} \leqslant 0 \qquad [1]$$

where p_c and p_t (both positive) are the cut-off pressure under hydrostatic compression and tension, respectively; q is defined the same as the von Mises equivalent stress $\overline{\sigma}$:

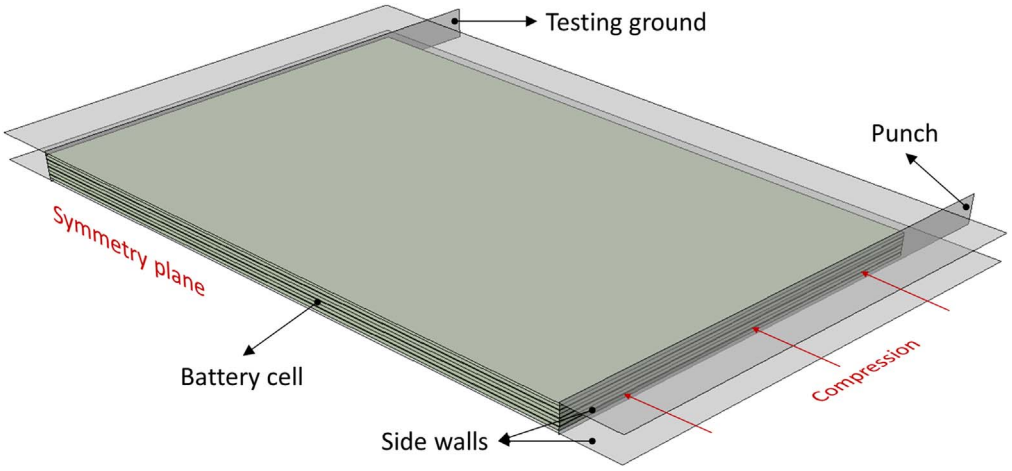

Figure 2. The finite element model of the in-plane compression test with a half symmetry.

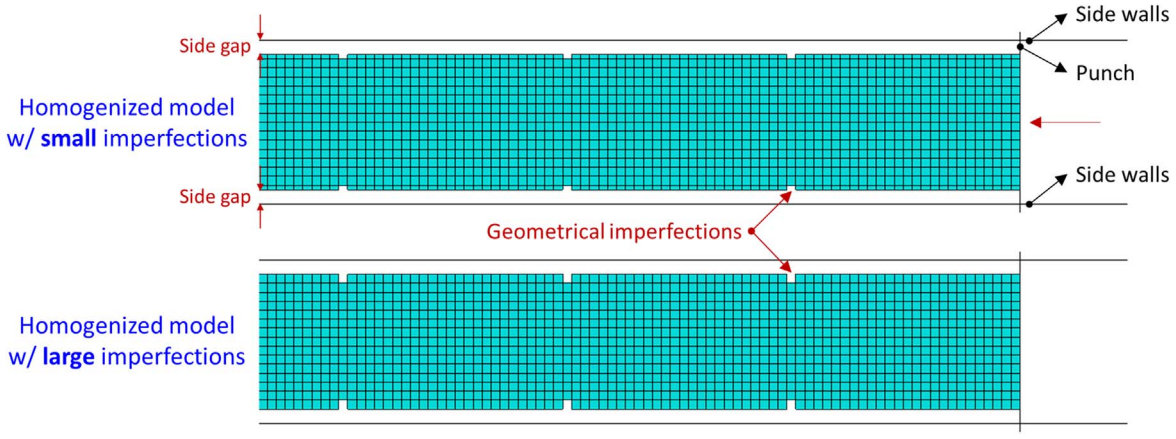

Figure 3. The zoom-in of the homogenized model of in-plane compression with imperfections of two sizes (small and large).

$$q = \overline{\sigma} = \sqrt{\frac{3}{2}\mathbf{s}:\mathbf{s}} = \sqrt{\frac{3}{2}}\|\mathbf{s}\| \quad [2]$$

where $\mathbf{s}$ is the stress deviator;

α is defined by:

$$\alpha = \frac{3k}{\sqrt{(3k_t + k)(3 - k)}} \quad [3]$$

where k and k_t are given as:

$$k = \frac{\sigma_c^0}{p_c^0} \text{ and } k_t = \frac{p_t}{p_c^0} \quad [4]$$

where σ_c^0 and p_c^0 are the initial yield stress under the uniaxial compression and the initial pressure under hydrostatic compression. A geometric illustration of these variables is shown in Fig. 5.

For battery cells, different from the original isotropic hardening of the Deshpande–Fleck model, volumetric hardening law is applied.[38] It implies that during the hardening, the yield stress under hydrostatic tension p_t keeps as a constant, while the yield stress under hydrostatic compression evolves:

$$p_t = \text{const.}; p_c = p_c(\varepsilon_v) \quad [5]$$

where ε_v is the volumetric compacting plastic strain, which controls the evolution of the yield surface in the p-q space, defined as the "equivalent" strain in the present study:

$$\varepsilon_v \equiv -\varepsilon_v^p \quad [6]$$

Due to the zero plastic Poisson's ratio, $\varepsilon_{axial}^p = \varepsilon_v^p$ holds under uniaxial compression condition; therefore, the volumetric hardening can be expressed by the uniaxial compression data[1,33,38]:

$$p_c(\varepsilon_v^p) = \frac{\sigma_c(\varepsilon_{axial}^p)\left[\sigma_c(\varepsilon_{axial}^p)\left(\frac{1}{\alpha^2} + \frac{1}{9}\right) + \frac{p_t}{3}\right]}{p_t + \frac{\sigma_c(\varepsilon_{axial}^p)}{3}} \quad [7]$$

where $\sigma_c(\varepsilon_{axial}^p)$ is the yield stress under the uniaxial compression test as a function of the absolute value of axial plastic strain.

The Deshpande–Fleck model is based on the non-associated flow rule and the flow potential is defined as:

$$\Phi' = \sqrt{q^2 + \frac{9}{2}p^2} \quad [8]$$

According to the flow rule, the plastic strain rate tensor is calculated by:

$$\dot{\boldsymbol{\varepsilon}}^p = \dot{\bar{\varepsilon}}^p \frac{\partial \Phi'}{\partial \boldsymbol{\sigma}} \quad [9]$$

where $\dot{\bar{\varepsilon}}^p$ is the equivalent plastic strain rate, which is defined by applying the work equivalence principle:

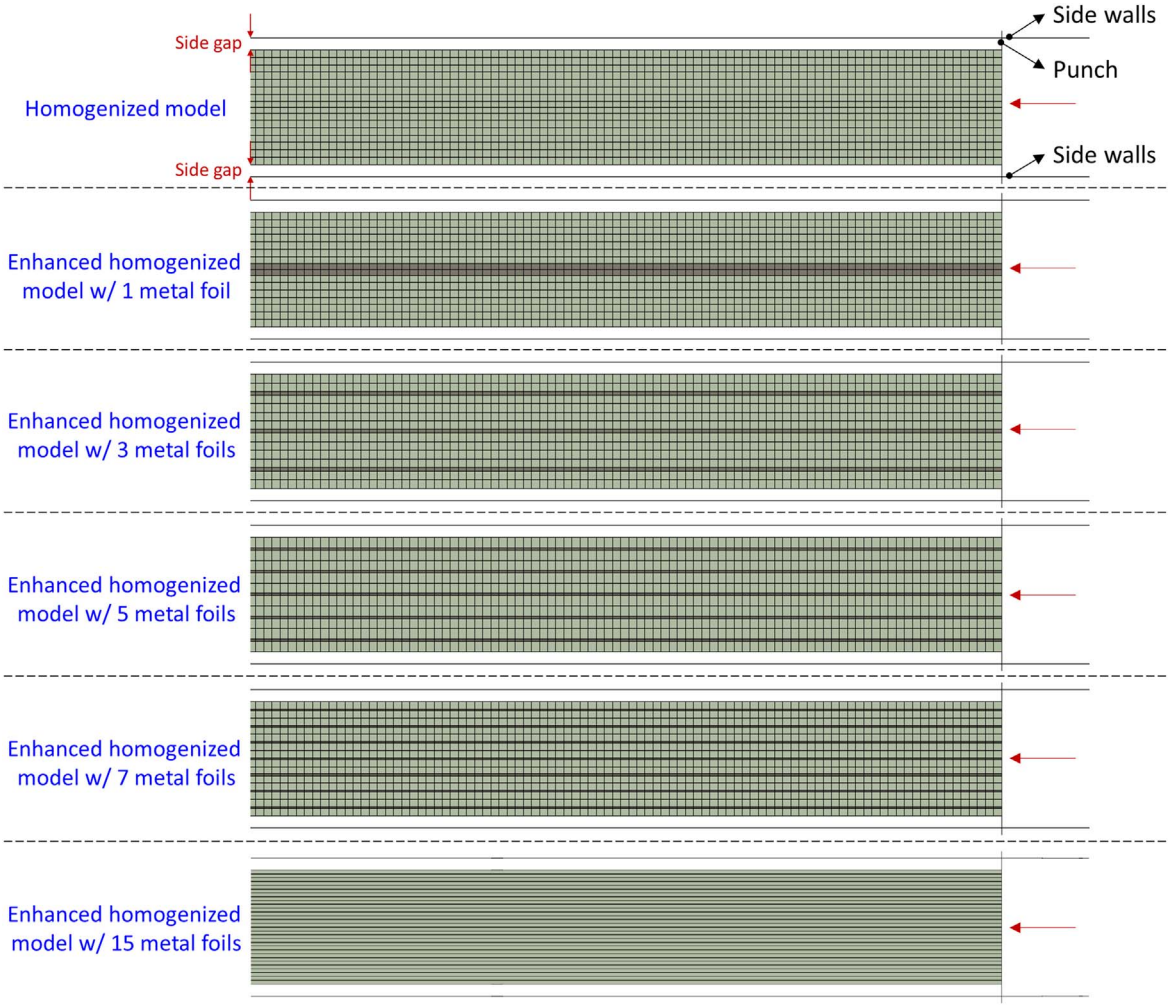

Figure 4. The zoom-in of the "enhanced homogenized model" of the in-plane compression with different configurations of the battery cells. Note that the illustration of the model with 15 metal foils are modified to indicate the layers (Color code: brown = coating material; gray = metal foil).

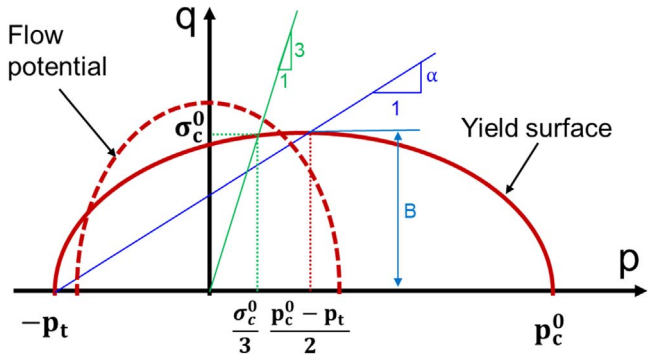

Figure 5. The schematic drawing of the yield criterion and the flow potential of the Deshpande–Fleck model in the *p-q* space.[33]

Table I. Material parameters for the homogenized model.

Young's modulus	Poisson's ratio	k	k_t	A	n
4.2 GPa	0	1	10	500 MPa	1.5

$$\dot{\bar{\varepsilon}}^{\mathrm{p}} = \frac{\boldsymbol{\sigma}\colon \dot{\boldsymbol{\epsilon}}^{\mathrm{p}}}{\Phi'} \qquad [10]$$

J2 plasticity model.—For the metal foils, the classic J2 Mises plasticity model is employed. The yield function is expressed in the following equation and in the p-q space, it is illustrated as a straight horizontal line, as it is independent of the pressure.

$$\Phi = q - \sigma_{\mathrm{Y}} \leqslant 0 \qquad [11]$$

where σ_{Y} is the yield stress. Besides, the metal foils follow the plastic incompressibility and associated flow rule.

Results

Material model calibration.—For the homogenized model, the parameter calibration procedure only involves the elastic properties and the two shape-controlling parameters in the Deshpande–Fleck model and the hardening curve of the cell, for which a power-law relation of the stress and the volumetric plastic strain, $\sigma = A\varepsilon_{\mathrm{v}}^{n}$ is employed. The calibration procedure of the plasticity parameters is detailed in the previous study. It uses the out-of-plane indentation tests with various punch shapes, including flat, cylindrical, and spherical punches. The calibrated parameters are listed in Table I. The comparison between the simulation prediction and the

experimental results on the out-of-plane flat-punch indentation test is shown in Fig. 6a.

For the enhanced homogenized model, there are two sets of material parameters to be calibrated, the equivalent metal foils and the coating materials. As the mechanical properties of the metal foils have already been identified and reported in the previous study, Young's modulus and the hardening behavior can be calculated by considering the average values weighted by the relative volume, defined by:

$$\begin{aligned} E_{\mathrm{Cu-Al}} &= \frac{V_{\mathrm{Cu}}}{V_{\mathrm{Cu}}+V_{\mathrm{Al}}}E_{\mathrm{Cu}} + \frac{V_{\mathrm{Al}}}{V_{\mathrm{Cu}}+V_{\mathrm{Al}}}E_{\mathrm{Al}}; \\ \sigma_{\mathrm{Y,\,Cu-Al}} &= \frac{V_{\mathrm{Cu}}}{V_{\mathrm{Cu}}+V_{\mathrm{Al}}}\sigma_{\mathrm{Y,\,Cu}} + \frac{V_{\mathrm{Al}}}{V_{\mathrm{Cu}}+V_{\mathrm{Al}}}\sigma_{\mathrm{Y,\,Al}} \end{aligned} \quad [12]$$

where E is Young's modulus; V is the volume, and the subscript Cu and Al stand for the Cu and Al foils. The individual and equivalent hardening curves for Cu and Al foils are shown in Fig. 6b.

With the parameters of the equivalent metal foils obtained, the parameter calibration for the equivalent coating materials is conducted by an inverse fitting to match the force–displacement response of the out-of-plane flat-punch indentation tests. To save the cost of the fitting procedure, the two parameters controlling the yield locus are not changed and only a scaling factor of the hardening curve is fitted. The predicted force–displacement curve by the enhanced homogenized models reaches a very good agreement with the experiments and the homogenized model by scaling down the hardening curve to 80%, as shown in Fig. 6a. The two hardening curves for the coating materials from homogenized model and enhanced homogenized model are also compared in Fig. 6c.

Homogenized model.—Under the assumption of deformation isotropy, with the calibrated material parameters from out-of-plane tests, the in-plane compression test simulation is conducted and the deformation history is shown in Fig. 7a. It is noted that the deformation history is measured by the nominal strain, which is defined by the current compression divided by the initial battery width, 150 mm.

It is clear that the deformation of the homogenized model is quite uniform until the compression reaches 10%, which is much longer than the experiments. As shown in Fig. 8,the predicted force shows a good agreement with the experiment at the first percentage of deformation. The prediction overestimates the experiments significantly when the buckling appears. The overshooting is attributed to primarily lacking of precise representation of the foldings. However, another possible reason could also be that the anisotropic behavior of the batteries play a role in the difference between in-plane and out-of-plane deformation.

Approach I: homogenized model with imperfection.—The force–displacement curves of the homogenized models with small and large imperfections are plotted together with the homogenized model without imperfections and experimental data in Fig. 8. Both sizes of the imperfections have only minor influences on the force responses. The pattern is reasonable as larger imperfections result in a more obvious reduction of the force. However, the overall response is still far beyond the experimental data. To also investigate the influence on the buckling effects, the deformation history of the simulation is plotted in Fig. 7b. The large imperfections are visible at the edges of the entire model and they do play a role during the deformation, as the stress/strain concentrate at these locations, once the deformation reaches a larger extent such as 5% and 10%. However, these local perturbations did not influence the overall buckling behavior of the entire structure. Comparing with the deformation history of the completely homogenized model shown in Fig. 7a, the buckling number and wavelength are very similar. What is different is that the imperfections do cause periodic shear bands, which are in a quite similar shape as the foldings observed in experiments. These shear bands cause the drop of the overall force but could not change the number of half-waves of buckling. It is therefore concluded that introducing the geometrical imperfections on a homogenized model could not resolve the mechanism of the buckling during the deformation process. A more severe triggering

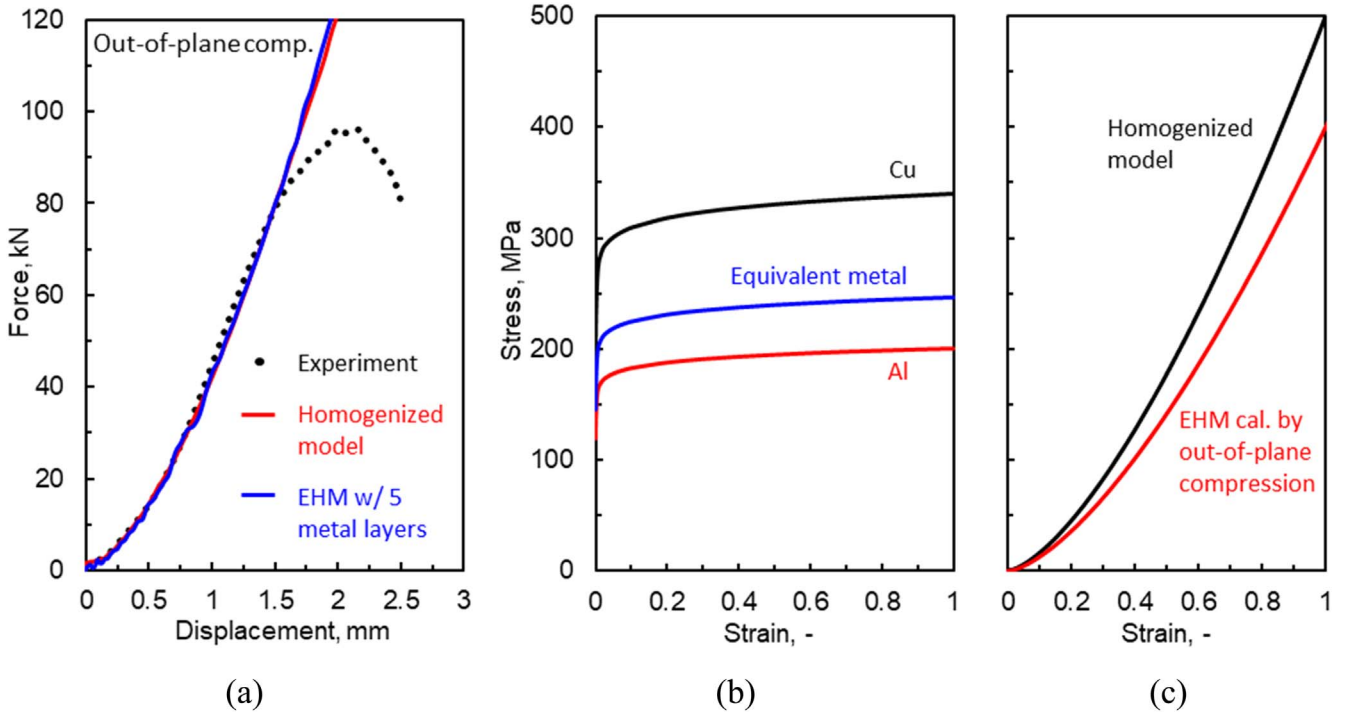

Figure 6. (a) Comparison of the force–displacement response of the out-of-plane flat-punch indentation test between experiments, homogenized model, and enhanced homogenized model; (b) the hardening curves for Cu foil, Al foil, and the equivalent metal foil; (c) the hardening curves of the homogenized model and the equivalent coating material in the enhanced homogenized models.

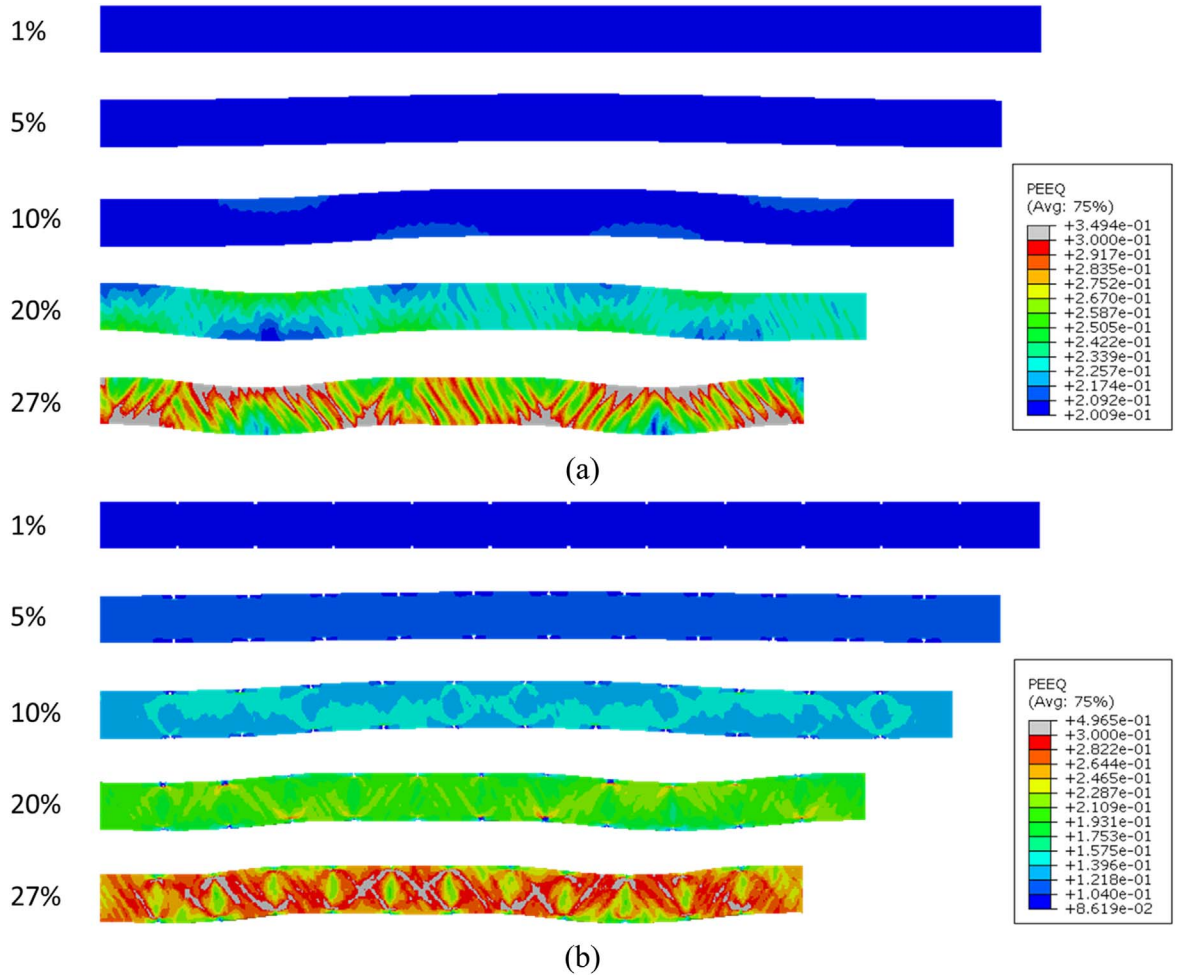

Figure 7. Deformation history of the in-plane compression simulation with the homogenized model (a) and the homogenized model with large imperfections (b).

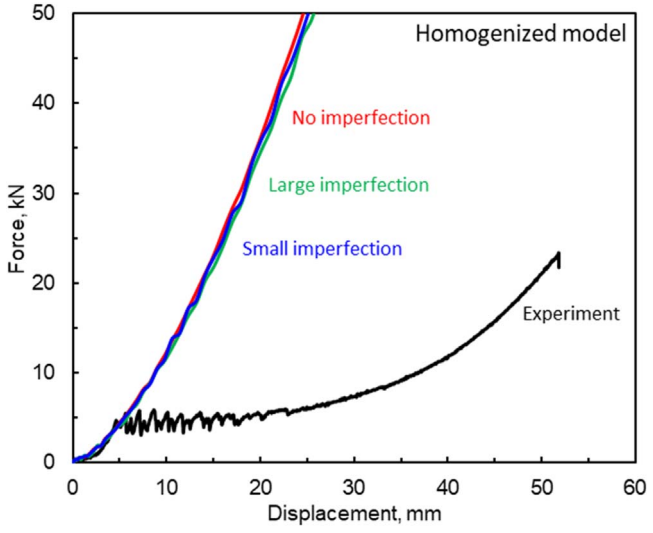

Figure 8. Comparison of the force–displacement response between the in-plane compression experiment and homogenized model without imperfection, with small and large imperfections.

mechanism based on the material inhomogeneity is needed for the representation of the buckling during in-plane compression.

Approach II: enhanced homogenized model.—All the five enhanced homogenized models (EHM) in Fig. 3 are run with the derived material parameters and the force–displacement curves of them are compared with the homogenized model as well as the experimental results in Fig. 9. Starting from the EHMwith only one metal foil, it overpredicts the force at the very beginning. This is attributed to the deformation of the metal foil, as the metal foil owns much higher yield stress and initial hardening rate than the coating material. The deformation history of the model with one metal foil is shown in Fig. 10 for Mises stress and equivalent strain contours. From the Mises stress plot, it is clear to see that the metal foil carries high and immediate stresses at the very beginning of deformation. For the equivalent strain, it is noticeable that the equivalent strain here has different meanings for the metal foils and coating materials. For the metal material, the equivalent strain is referred to as the Mises equivalent plastic strain, while for coating materials it is the plastic volumetric strain. Although different quantities are referred to, it can still be seen that the coating materials carry more deformation from the equivalent strain contour during the deformation. Overall, folds are formed early enough compared to the homogenized models. Buckling is triggered by the metal foil and then transmitted to the coating materials. Due to the loose contact between them, the buckling of the whole structure is not so similar to the experiments. A fewer number of folds are formed and unrealistic deformation is also found on the left end of the battery. This is again because the frictionless contact was applied.

When the number of the metal foils is increased, a clear decrease in the force is present, especially at the beginning of the deformation. When the number of layers becomes five or seven, the force shows a good agreement with the experiments up to 10 mm compression. Afterward, the numerical simulation overestimates

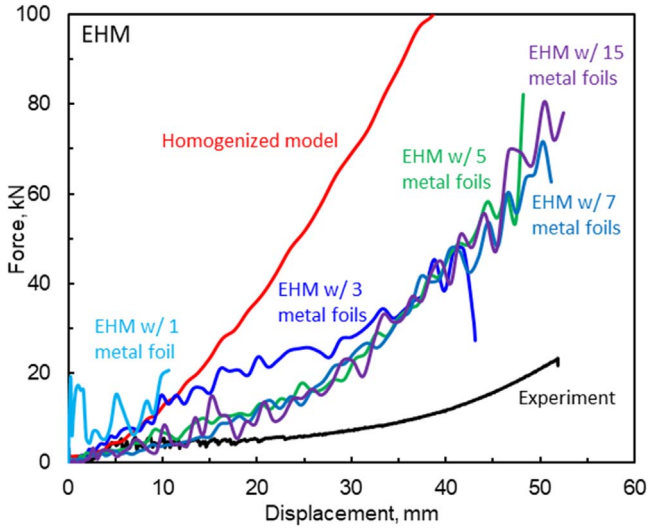

Figure 9. Comparison of the force–displacement response between the in-plane compression experiment and the enhanced homogenized models with varied numbers of metal foils.

intensified and the final pattern of the folds corresponds very well to the experiments in terms of both fold number and the wavelength. In terms of the stress distribution, it can be seen that with more metal layers, a slightly increased stress concentration is observed within the folds, but the magnitude is limited. The same conclusion can be drawn as for the force–displacement responses when the number of metal layers reaches five, the buckling and fold formation of the structure can be reproduced with enhanced homogenized models.

Discussion

Influence of the gap distance.—In the previous section, the gap distance between the battery cell and the side walls were modeled with the experimental measurement. However, it is easy to imagine that the mechanical responses of the system are strongly dependent on the gap distance between the battery cells and the side walls. Therefore, in this section, a parametric study is performed by varying the gap distances from 0.8 mm to 0.6 mm, 0.4 mm, and 0.2 mm. The enhanced homogenized model with five metal foils is chosen for the study, as it gives converged force–displacement response as well as the right number of folds. The force–-displacement response of the model with different gap distances is given in Fig. 12. It is obvious that the force response increases with the decrease of the gap distance. In addition to the absolute force

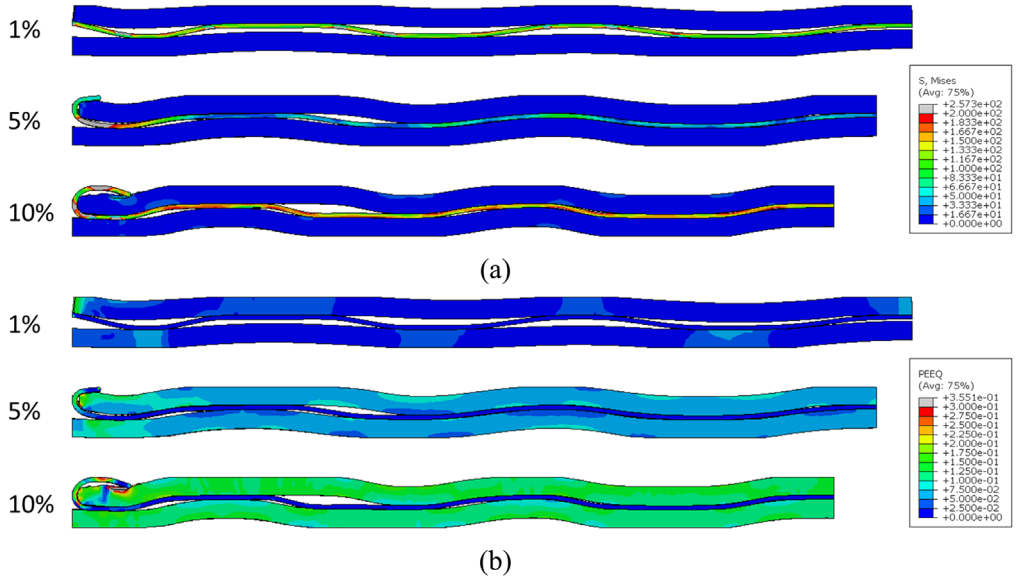

Figure 10. Deformation history of the in-plane compression simulation of the enhanced homogenized model with one layer of equivalent metal in the Mises stress contour (a) and the equivalent strain contour (b).

the force by a factor of 2–3 at the end of the deformation. It is interesting to conclude that the enhanced homogenized models with different metal foils converge when the metals layers are above five, which is validated by the results of a model with 15 metal layers.

The deformation history of these models is shown in Fig. 11, together with the experimental observation at 15% and 30% deformation. It can be seen that at 5% deformation, a general macro buckling is formed for all the models. With the deformation, many local buckles and folds are gradually formed. This is different from the experimental observation, as a progressive folding pattern was revealed in the experiments. It is expected that the sequence of the folding formation is highly related to the friction between the battery cells and the side walls as well as the contact between all the layers. Although the frictionless contact makes the deformation less realistic for the model with few metal foils, for the model with metal foils more than three, the local folds of the layers are already well presented by the global structure. At 15% deformation, similar to the experimental observation, all the folds are formed for the models with more metal layers. At 30% deformation, the folds are heavily

values, the slope of the force increase has been raised with the decrease of the gap distance. To also reveal the difference in deformation behavior, the deformed battery at 20% of the in-plane compression is shown in Fig. 13 for various gap distances. It can be observed that the fold number is increased with the decrease of the gap distances. The model with a gap distance of 0.8 mm shows the correct fold number as the experiments, 11–12 folds, while the model with a gap distance of 0.2 mm shows about 20 folds. It can also be noticed with increasing gap distance, the deformed battery tends to be thicker, as the entire deformation range is increased with larger gaps. Form the deformation behavior, it is also clearly seen that battery with smaller gaps shows higher local stresses especially for the metal foils, which is contributing to a higher global force response as shown in Fig. 12.

Influence of the mesh size.—In the previous section, all the simulations were conducted using rather coarse mesh, as shown in Fig. 14. The element size for the coarse mesh is about 0.5 mm × 0.5 mm for the coating material, while for metal foils, the height of

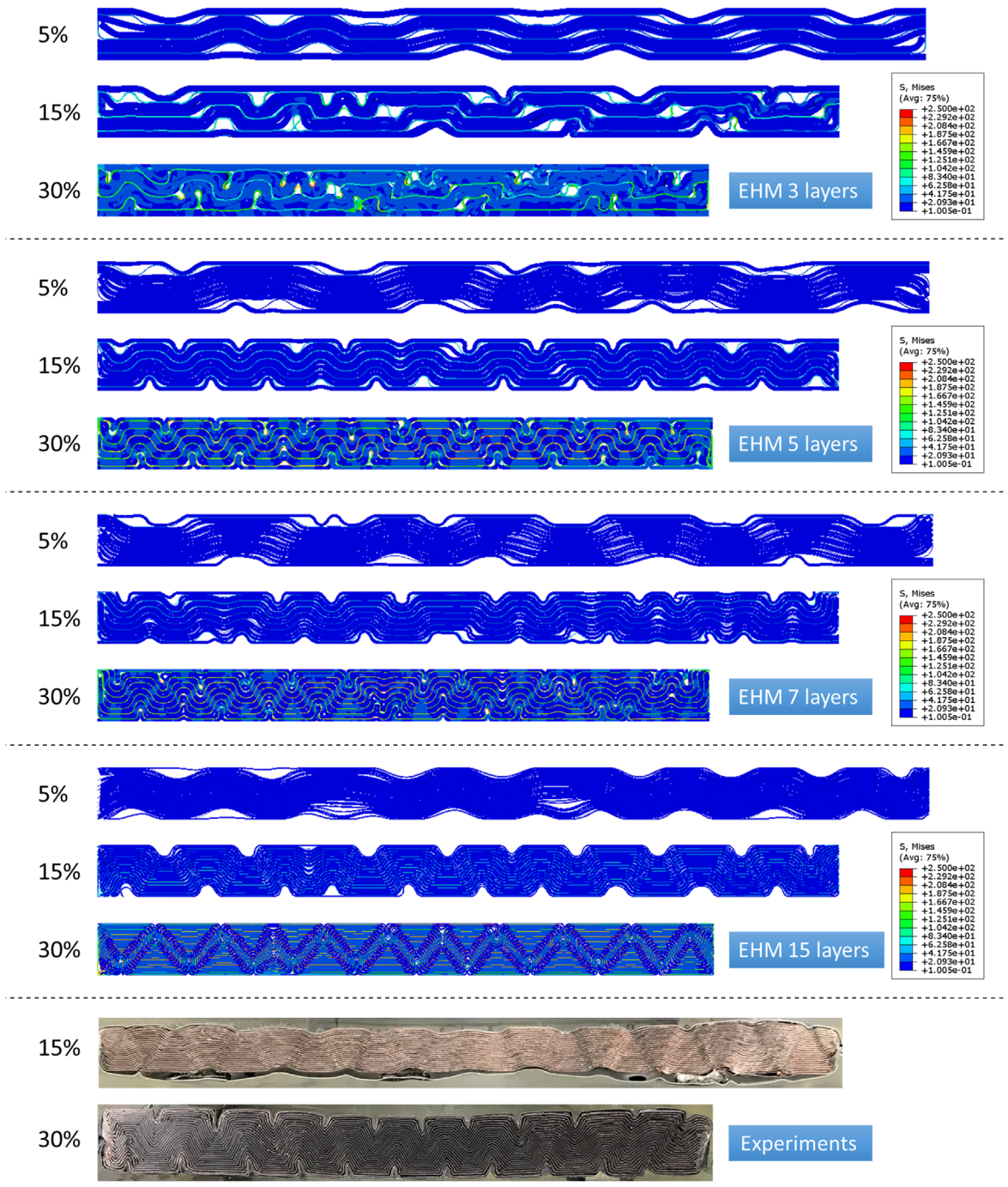

Figure 11. Deformation history of the in-plane compression simulation of the enhanced homogenized model with 3, 5, 7, and 15 layers compared with the experimental observations.

the element is restricted by the foil, so it is normally smaller than 0.5 mm, while the width of the element is 0.5 mm. This mesh was taken as it gives reasonably good computational time. To reveal the mesh influence on the system responses, a finer mesh is created as shown in Fig. 14. The element for the fine mesh is featuring a size of 0.25 mm $\times$ 0.25 mm.

The force–displacement responses of the model with two different mesh sizes are shown in Fig. 15. The fine mesh shows a softer mechanical behavior than the coarse one, resulting also a slightly closer prediction of the experimental results. It is worth mentioning that the prediction is in a good agreement with the experiments within the in-plane displacement of 15 mm. The deformation patterns of the enhanced homogenized model with two different mesh sizes are also shown in Fig. 16. Different from the regular fold formation in the coarse mesh, the folds formed in the fine mesh have a less stable pattern and also a fewer number than the experiments. It is suggesting that finer mesh creates more flexibility for the local deformation, which implies that the enhanced homogenized model with five metal foils might not reach a convergence of the fold formation yet for the fine mesh and an improved deformation pattern is shown for the enhanced homogenized model with seven metal layers. Therefore, for finer mesh configuration, models with more metal foils shall be further conducted. However, it should be noted that the mesh control only slightly contributes to the improvement of the prediction but will not completely bring the force to the experimental level.

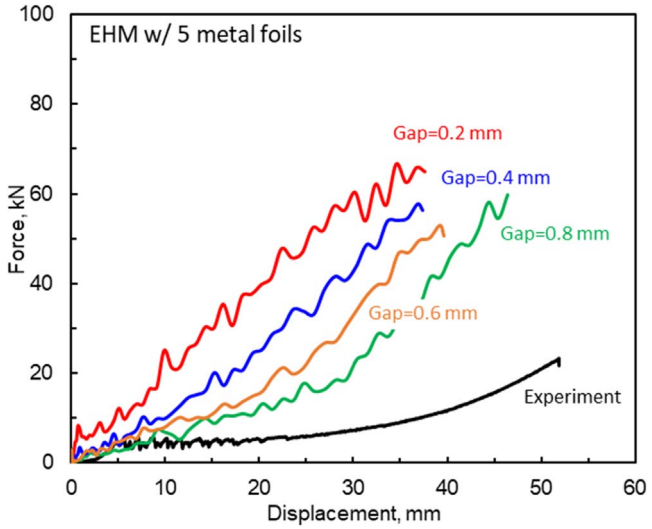

Figure 12. Comparison of the force–displacement response between the in-plane compression experiment and the enhanced homogenized models (5 metal foils) with different gap distances.

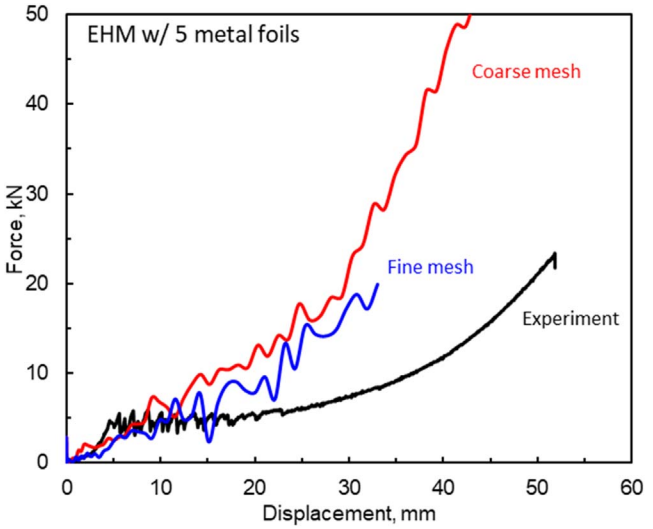

Figure 15. Comparison of the force–displacement response between the in-plane compression experiment and the enhanced homogenized models (5 metal foils) with coarse and fine meshes.

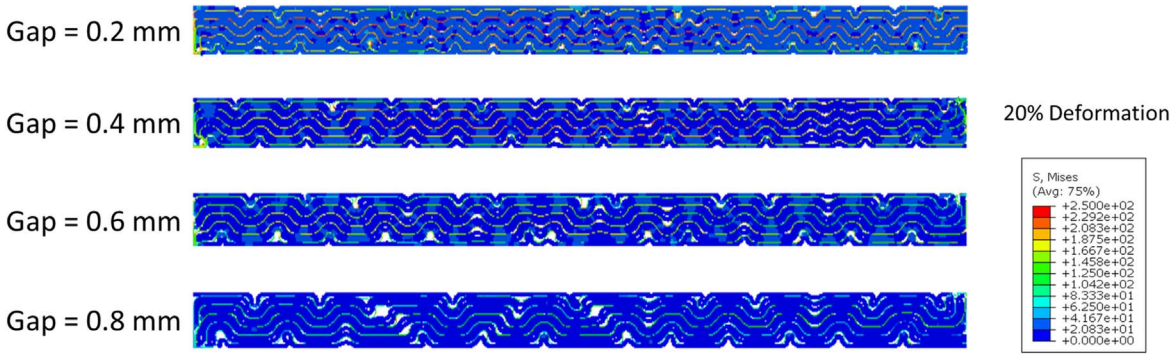

Figure 13. Deformation at 20% in-plane compression of the enhanced homogenized model (5 metal foils) with different gap distances.

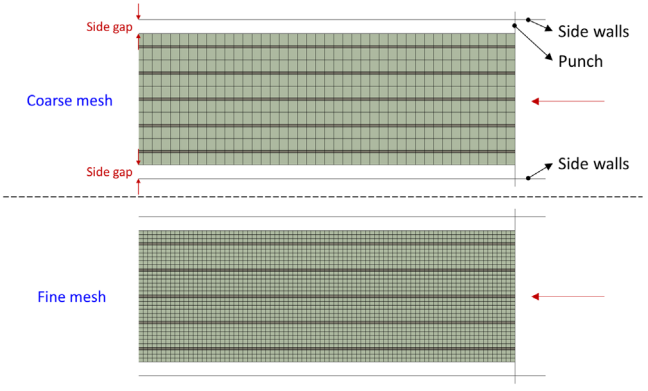

Figure 14. Zoom-in view of the enhanced homogenized model (5 metal foils) with coarse and fine mesh.

Influence of the contact between layers.—One of the assumptions made in the study is that the layers of both the coating and the metals are able to be detached from each other. The assumption is rather creating a lower-bound condition, especially at the beginning of the deformation. The opposite condition for the fully detached case is the fully bonded one, i.e. all the layers are completely tied together, and any detachment or relative displacement is not allowed. This case is creating an upper-bound solution for the in-plane compression problem. The force–displacement responses for these two cases are shown in Fig. 17. As expected, the fully bonded case shows a very high initial force due to its rigid restriction. The force drops to a level similar to the experiments and the fully detached case once the folds are formed at about 5 mm displacement. After a short range of overlap between the two cases, the fully bonded case has overestimated the force significantly after the displacement of about 10 mm. The increase is in a linear form until it reaches about 45 mm displacement, at which the two cases almost converge.

The deformation patterns at the 27% compression of these two cases are shown in Fig. 18. It is clear to see that the fully bonded case shows very distinct folds, but the number of progressive folds is fewer than the experiments and the fully detached case. The local relative movement is fully restricted for the fully bonded cases compared to the detached one, which is the reason for the much higher local stress concentration, especially in the metal foils. This, in general, is contributing to the higher global forces. However, at the folds, the fully bonded case creates more severe deformation, as the folds are deeper, which would cause a lower force as seen at the very late phase of the deformation. In general, a better folding condition can be reached by increasing the metal foils, as seen in Fig. 9. In this sense, a model with more metal foils but still fully detached might give a more realistic prediction for the in-plane compression.

Anisotropy of the coating materials.—After the attempts with different numerical configurations, the deformation pattern of buckling and folding is quite well predicted, while the force–-displacement response remains overestimated. The substantial

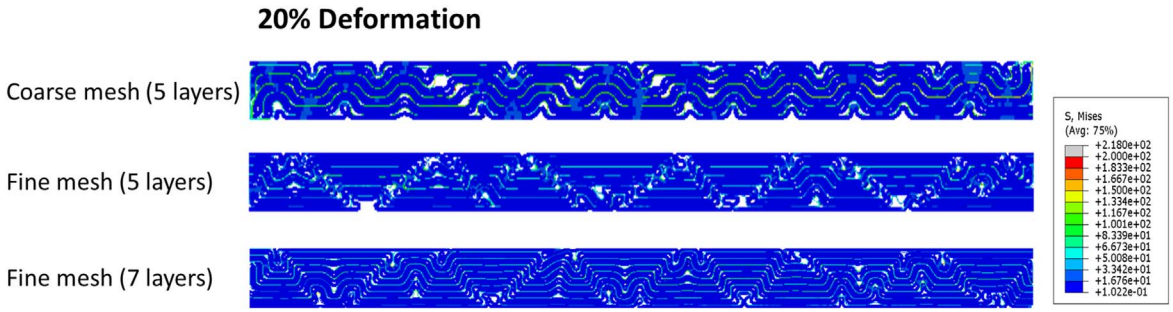

Figure 16. Deformation at 20% in-plane compression of the enhanced homogenized model with coarse and fine meshes.

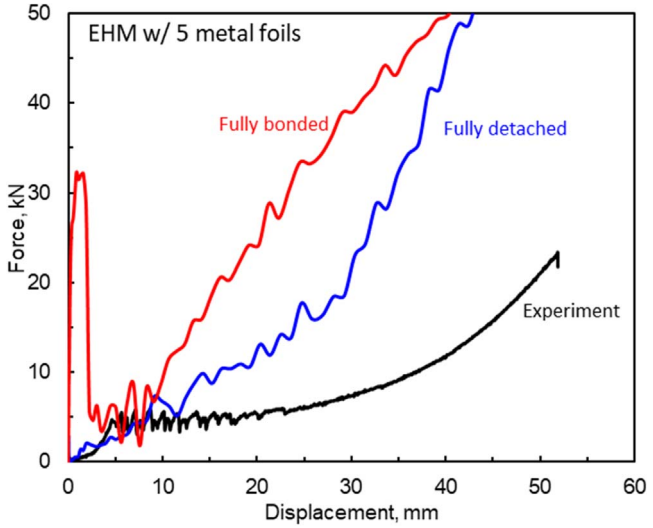

Figure 17. Comparison of the force–displacement response between the in-plane compression experiment and the enhanced homogenized models (5 metal foils) with fully bonded and fully detached configurations.

compression, as shown in Fig. 19b. It is, therefore, concluded that the dominant factor for the overestimation of the force in the in-plane compression test is very likely to be the anisotropy of the coating material. The root for it should be correlated to the deformation-induced anisotropy to the granular materials during the production and assembly of pouch cells when pressure and deformation are enforced in the out-of-plane direction. To better understand and simulate this problem, the investigating team has committed to follow-up experimental work and formulation of an anisotropic material model for the coating materials in pouch cells.

Conclusions

From the study of the in-plane compression test of a large-size battery cell, the following conclusions can be drawn:

- For the fully constrained uniform in-plane compression tests, no short circuit is observed. The compression triggers the cells to buckle and develops progressive folding, similarly as a prismatic column under axial compression. To represent the mechanism of buckling in the finite element model is critical for the in-plane compression simulation.
- The completely homogenized model overpredicts the force level due to its incapability to reproduce the right number of folds. Two approaches are developed to trigger the buckles, homogenized models with imperfections and enhanced homogenized model with equivalent metal layers.
- The imperfections in the homogenized model show only minor effects on the overall force–displacement responses compared to the fully homogenized model. It also has limited effects on the formations of buckles still leading fewer folds compared to the experiments.
- The enhanced homogenized model, on the contrary, offers a good combination of reflecting the physics and computational benefits. With the number of metal foils over five, the correct folding moment and fold number are predicted. It also predicts the force level at a reasonable level at the beginning of the tests but still overestimates the force at the latter stage of deformation.
- Based on a parametric study on the gap distance, mesh size, and layer interaction, the choice of gap distance and the layer interaction in the study are creating a lower-bound solution to

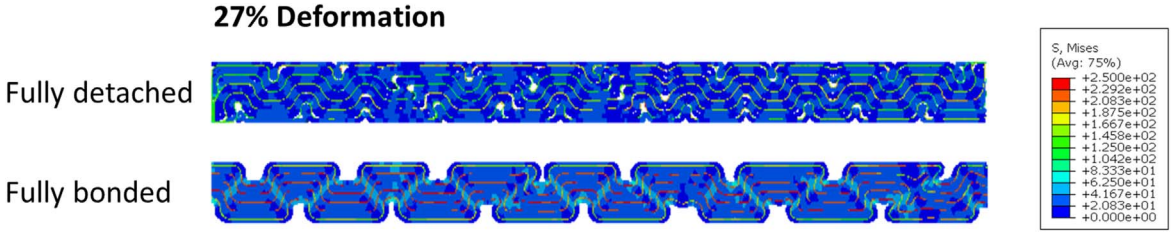

Figure 18. Deformation at 27% in-plane compression of the enhanced homogenized model (5 metal foils) with fully detached and fully bonded configurations.

overestimation of the force but with the right deformation pattern implies that the assumption of deformation isotropy might not be valid for the pouch cells. It is a prerequisite for a possible parameter fitting procedure by using the out-of-plane compression tests, but not a necessary condition for the cells.

In this section, we are focusing on the improvement of the prediction of force–displacement response of the in-plane compression tests by introducing deformation anisotropy. However, as we only have out-of-plane and in-plane compression data, it is not possible to formulate and calibrate a comprehensive anisotropic Deshpande–Fleck model, which is also beyond the scope of the current work. Therefore, a simple inverse engineering approach is implemented to fit the overall force–displacement response of the in-plane compression by changing the hardening curve of the equivalent coating material. After a successful agreement between the simulation and experiments, as shown in Fig. 19a, it is seen that the hardening behavior of the equivalent coating material in in-plane compression needs to be significantly smaller than the out-of-plane

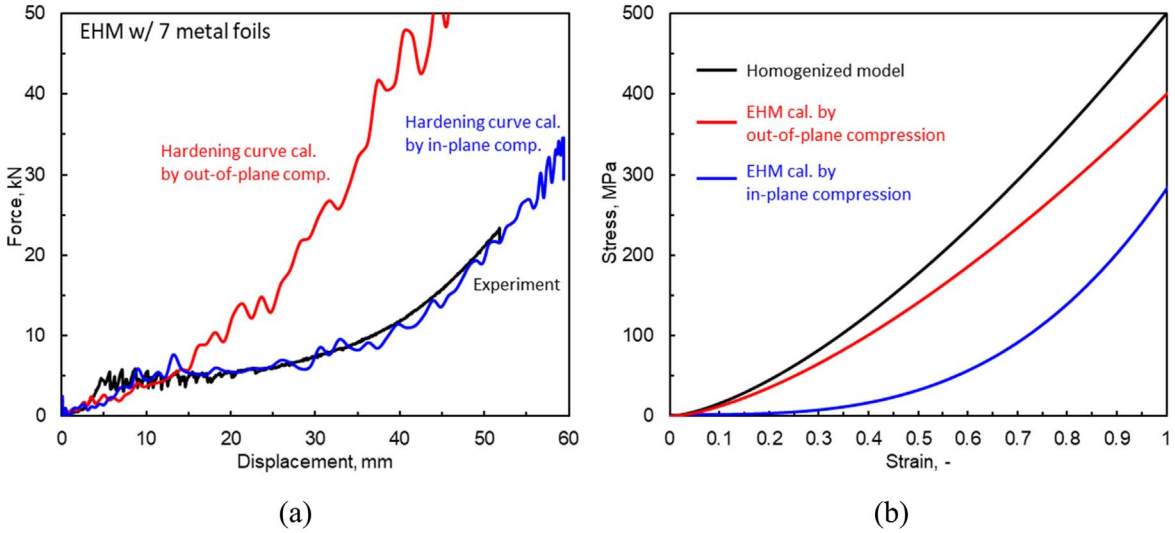

Figure 19. (a) Comparison of the force–displacement response between the in-plane compression experiment and the enhanced homogenized models (7 metal foils) with the hardening curves by out-of-plane and in-plane compression tests; (b) comparison of the hardening curves of the homogenized model, the enhanced homogenized model calibrated by the out-of-plane and in-plane compression tests.

the problem. Finer mesh could lead to a reduction of the force response, but its effect will be still limited and the computational cost is too high.

- The reason responsible for the mismatch between the prediction and the experiments is very likely to be the deformation anisotropy of the coating materials. With an inverse engineering method, a very good agreement of the force–displacement response between the experiment and simulation is reached. The resultant hardening curve for the equivalent coating materials in the in-plane compression turned out to be significantly lower than that for the out-of-plane compression tests. The root of it can be correlated to the pre-deformation in the out-of-plane direction of the lithium-ion pouch cells during the production and assembly processes.

Acknowledgments

The authors are grateful to the MIT Battery Modeling Consortium (Altair, AVL, Boston-Power, Daimler, Jaguar-Land Rover, LG Chem, Murata, and PSA Groupe) and Ford-MIT Alliance for financial support. The CSC – IT Center for Science in Finland is acknowledged for providing computational power under project number 2001353.

ORCID

Junhe Lian https://orcid.org/0000-0003-0323-3486
Juner Zhu https://orcid.org/0000-0001-7072-2293

References

1. Y. Xia, T. Wierzbicki, E. Sahraei, and X. Zhang, *J. Power Sources*, **267**, 78 (2014).
2. S. H. Chung, T. Tancogne-Dejean, J. Zhu, H. Luo, and T. Wierzbicki, *J. Power Sources*, **389**, 148 (2018).
3. J. Zhu, X. Zhang, T. Wierzbicki, Y. Xia, and G. Chen, Structural Designs for Electric Vehicle Battery Pack against Ground Impact, in, SAE International (2018).
4. T. Kisters, E. Sahraei, and T. Wierzbicki, *Int. J. Impact Eng.*, **108**, 205 (2017).
5. E. Sahraei, M. Kahn, J. Meier, and T. Wierzbicki, *RSC Adv.*, **5**, 80369 (2015).
6. E. Sahraei, J. Meier, and T. Wierzbicki, *J. Power Sources*, **247**, 503 (2014).
7. T. Wierzbicki and E. Sahraei, *J. Power Sources*, **241**, 467 (2013).
8. E. Sahraei, R. Hill, and T. Wierzbicki, *J. Power Sources*, **201**, 307 (2012).
9. E. Sahraei, J. Campbell, and T. Wierzbicki, *J. Power Sources*, **220**, 360 (2012).
10. D. Finegan, B. Tjaden, T. Heenan, R. Jervis, M. Di Michiel, A. Rack, G. Hinds, D. Brett, and P. Shearing, *J. Electrochem. Soc.*, **163**, A3285 (2017).
11. J. Zhu, X. Zhang, E. Sahraei, and T. Wierzbicki, *J. Power Sources*, **336**, 332 (2016).
12. M. Y. Ali, W.-J. Lai, and J. Pan, *J. Power Sources*, **273**, 448 (2015).
13. C. M. Amodeo, M. Y. Ali, and J. Pan, *Int. J. Crashworthiness*, **22**, 1 (2017).
14. M. Y. Ali, W.-J. Lai, and J. Pan, *J. Power Sources*, **242**, 325 (2013).
15. W.-J. Lai, M. Y. Ali, and J. Pan, *J. Power Sources*, **245**, 609 (2014).
16. W.-J. Lai, M. Y. Ali, and J. Pan, *J. Power Sources*, **248**, 789 (2014).
17. A. J. Mason, in, MIT (2017).
18. G. Kermani, B. Dixon, and E. Sahraei, *Energy Science & Engineering*, **7**, 890 (2019).
19. J. Zhu, W. Li, T. Wierzbicki, Y. Xia, and J. Harding, *Int. J. Plasticity*, **121**, 293 (2019).
20. Z. Pan, W. Li, and Y. Xia, *Journal of Energy Storage*, **27**, 101016 (2020).
21. L. Wang, S. Yin, and J. Xu, *J. Power Sources*, **413**, 284 (2019).
22. J. Zhu, T. Wierzbicki, and W. Li, *J. Power Sources*, **378**, 153 (2018).
23. R. Hill, *J. Mech. Phys. Solids*, **11**, 357 (1963).
24. W. Liu, J. Lian, N. Aravas, and S. Münstermann, *Int. J. Plasticity*, **126**, 102614 (2020).
25. J. Lian, W. Liu, F. Shen, and S. Muenstermann, *Proceedings of the 20th International Esaform Conference on Material Forming (Esaform 2017)*, p. 020030 (2017).
26. Q. Xie, A. Van Bael, Y. G. An, J. Lian, and J. J. Sidor, *Mater. Sci. Eng. A*, **721**, 154 (2018).
27. Q. Xie, S. Gorti, J. J. Sidor, Y. G. An, Y. D. Wang, J. Lian, H. Lan, and K. An, *Steel Res. Int.*, **89**, 1700408 (2018).
28. J. Lian, H. Yang, N. Vajragupta, S. Münstermann, and W. Bleck, *Comput. Mater. Sci.*, **94**, 245 (2014).
29. Q. Xie, J. Lian, F. Sun, B. Gan, and Y. Wang, *The Journal of Strain Analysis for Engineering Design*, **53**, 353 (2018).
30. Q. Xie et al., *Acta Mater.*, **193**, 138 (2020).
31. E. Sahraei, E. Bosco, B. Dixon, and B. Lai, *J. Power Sources*, **319**, 56 (2016).
32. C. Zhang, J. Xu, L. Cao, Z. Wu, and S. Santhanagopalan, *J. Power Sources*, **357**, 126 (2017).
33. X. Zhang and T. Wierzbicki, *J. Power Sources*, **280**, 47 (2015).
34. J. Lian, T. Wierzbicki, J. Zhu, and W. Li, *Eng. Fract. Mech.*, **217**, 106520 (2019).
35. J. Zhu, M. Koch, J. Lian, W. Li, and T. Wierzbicki, *J. Electrochem. Soc.*, **167**, 090533 (2020).
36. W. Liu, J. Lian, S. Münstermann, C. Zeng, and X. Fang, *Int. J. Mech. Sci.*, **176**, 105534 (2020).
37. V. S. Deshpande and N. A. Fleck, *J. Mech. Phys. Solids*, **48**, 1253 (2000).
38. ABAQUS, *Documentation*, Dassault Systems (2017).